



Cite this: *Phys. Chem. Chem. Phys.*,
2024, 26, 21379

Extension of the D3 and D4 London dispersion corrections to the full actinides series[†]

Lukas Wittmann, ^{‡,a} Igor Gordiy, ^{‡,a} Marvin Friede, ^{‡,a} Benjamin Helmich-Paris, ^b Stefan Grimme, ^a Andreas Hansen ^{*,a} and Markus Bursch ^{*,bc}

Efficient dispersion corrections are an indispensable component of modern density functional theory, semi-empirical quantum mechanical, and even force field methods. In this work, we extend the well established D3 and D4 London dispersion corrections to the full actinides series, francium, and radium. To keep consistency with the existing versions, the original parameterization strategy of the D4 model was only slightly modified. This includes improved reference Hirshfeld atomic partial charges at the ω B97M-V/ma-def-TZVP level to fit the required electronegativity equilibration charge (EEQ) model. In this context, we developed a new actinide data set called AcQM, which covers the most common molecular actinide compound space. Furthermore, the efficient calculation of dynamic polarizabilities that are needed to construct C_6^{AB} dispersion coefficients was implemented into the ORCA program package. The extended models are assessed for the computation of dissociation curves of actinide atoms and ions, geometry optimizations of crystal structure cutouts, gas-phase structures of small uranium compounds, and an example extracted from a small actinide complex protein assembly. We found that the novel parameterizations perform on par with the computationally more demanding density-dependent VV10 dispersion correction. With the presented extension, the excellent cost-accuracy ratio of the D3 and D4 models can now be utilized in various fields of computational actinide chemistry and, e.g., in efficient composite DFT methods such as r^2 SCAN-3c. They are implemented in our freely available standalone codes (dftd4, s-dftd3) and the D4 version will be also available in the upcoming ORCA 6.0 program package.

Received 13th April 2024,
Accepted 15th July 2024

DOI: 10.1039/d4cp01514b

rsc.li/pccp

1 Introduction

In computational chemistry, mean-field (MF) methods are very often the method of choice for the computation of the electronic and geometric structure of large systems. Some prominent members are Hartree–Fock theory, Kohn–Sham (KS) density functional theory (DFT), and semi-empirical extended tight-binding (TB) methods. However, a general problem of mean-field methods is the inability to describe long-range correlation effects, which are important to obtain correct energetic properties and geometries for many chemical problems.¹ The most significant long-range correlation effect is the London dispersion interaction,^{2–5} which is not only important for

non-covalent interactions (NCI),^{6,7} but also crucial for an accurate description of general thermochemistry,^{8,9} and even polarized systems that are expected to be dominated by electrostatic interactions (e.g., water clusters).^{10–13} Therefore, dedicated London dispersion corrections are necessary. This also applies to classical methods like force fields, where long-range dispersion effects need to be explicitly taken into account.¹⁴ Some of the popular models to describe long-range dispersion effects are the D3^{15,16} and D4^{17–19} corrections, Vydrov's and van Voorhis' VV10²⁰ model, including rVV10²¹ and NL,^{22,23} the exchange-dipole moment (XDM) method,^{24–26} or the Tkatchenko–Scheffler (TS) method.^{27,28} Specifically, the efficient DFT-D_n approach has proven to be reliable in countless quantum chemical applications and workflows.^{29,30} It is also very often already out-of-the-box combined with modern density functionals of all rungs.^{31–33}

Due to the ever-growing interest in larger systems with hundreds to thousands of atoms, the need for efficient methods is increasing. In this regime of computational chemistry, method selection is significantly influenced by cost considerations. Popular choices are QM/MM schemes,³⁴ combining a higher-level method in the areas of interest with a lower-level

^a Mulliken Center for Theoretical Chemistry, Universität Bonn, Beringstr. 4, 53115 Bonn, Germany. E-mail: hansen@thch.uni-bonn.de

^b Max-Planck-Institut für Kohlenforschung, Kaiser-Wilhelm-Platz 1, 45470 Mülheim an der Ruhr, Germany. E-mail: bursch@kofo.mpg.de

^c FACCTS GmbH, 50677, Köln, Germany

[†] Electronic supplementary information (ESI) available: All parameters for the DFT-D3, DFT-D4, and EEQ extensions, investigation of relativistic effects, and the complete AcQM set. See DOI: <https://doi.org/10.1039/d4cp01514b>

[‡] These Authors contributed equally.



method for the surroundings; composite methods,^{35–41} augmenting fast DFT methods with systematic corrections; or semi-empirical methods^{42–44} that significantly reduce the computational cost by introducing systematic approximations. In these approaches, the usage of, *e.g.*, the density-based DFT-NL scheme is not applicable because (i) it requires a reasonably accurate electron density and (ii) it is computationally expensive. Nonetheless, describing long-range dispersion effects is crucial, especially for larger systems, which are the primary application of efficient computational methods. Hence, there is a need for cost-effective dispersion corrections like the D3 and D4 models, which are employed in contemporary efficient methods including the GFN-FF force-field¹⁴ and the extended tight-binding GFN n -xTB methods.^{45–47} Accordingly, all workflows and tasks utilizing these efficient methods also depend on the availability of the respective D3 or D4 parameterizations. This, for example, includes conformer generation with the sophisticated conformer-rotamer-ensemble sampling tool CREST,^{48,49} fast transition-state sampling,⁵⁰ or QM/MM approaches like ONIOM^{34,51,52} (see Fig. 1).

Due to the progress of modern computational chemistry, the investigation of very large systems has become possible, which has naturally extended the field of application to the complex field of biochemistry.^{53–56} The rich chemistry of actinides, in particular, has attracted attention due to their unique chemical properties, applications and role in nature.⁵⁷ This part of (bio)chemistry studies, *e.g.*, the efficient disposal of nuclear waste from nuclear power plants and dismantled nuclear weapons,^{58–61} environmental effects of naturally occurring or accidentally released actinides,^{62,63} the interactions of metals with organic species, for example, on metalloenzymes and biomimetic compounds,^{64–67} the metabolic and biological

processes involving actinides^{68–70} – like their interaction with proteins,⁷¹ also in humans.^{70,72,73} In analytical (bio)chemistry, actinides are also already used,⁷⁴ for example for bio-imaging^{75,76} by using nanoparticles,⁷⁷ or radioimmunoassays.⁷⁸ Moreover, actinides find utility in medicine, particularly in nuclear medicine,⁷⁹ where they are utilized for, *e.g.*, radiopharmaceutical imaging and therapeutic applications.^{80,81}

However, due to the danger posed by the radioactivity of these elements and heavy metals in general, laboratory testing can be difficult. Therefore, theoretical research becomes invaluable in this context. Computational studies offer a safe and environmentally friendly alternative, enabling the prediction and avoidance of potential risks and hazardous substances before their large-scale application.⁸² The theoretical investigation can help to obtain a deeper understanding of the structure and reactivity of various bioorganic compounds, allowing for a systematic construction of biomimetics, which is the imitation of models, systems, and elements of nature for the purpose of solving complex human problems. In many cases, theoretical approaches are already accurate enough to allow comparison with experimental findings. Numerous theoretical works have been successfully published, offering valuable insights into various issues.^{83,84} The scope of application already ranges from investigations of the coordination chemistry of actinides,⁸⁵ their oxides and nitrides,^{86–88} surface adsorption processes,⁸⁹ to the investigation of complex properties,⁹⁰ up to larger complexes and materials.⁹¹ Also, already more far-reaching problems like the optimization of radioactive waste transmutation were investigated theoretically.⁹² Even the role of dispersion interactions for actinide chemistry has already been investigated in some studies, which showed better agreement with the experiment.⁹³

The efficient quantum chemical investigation of large actinide structures using mean-field methods is greatly limited by the availability of efficient dispersion corrections. The density-dependent schemes of Vydrov and van Voorhis and the XDM dispersion correction can be used combined with higher, much more expensive levels of theory, but no efficient solutions for semi-empirical methods are available.

With this work, we aim to extend our DFT-D3 and -D4 schemes to the full actinides series. This expansion will not only allow the existing DFT-D3 and -D4 density functionals to be applied to actinides but will also facilitate the adaptation of composite methods and various semi-empirical approaches to the entire series. We will begin by detailing the theory and implementation, followed by a description of the parameterization protocol. The final section will showcase the efficacy of the current dispersion correction schemes.

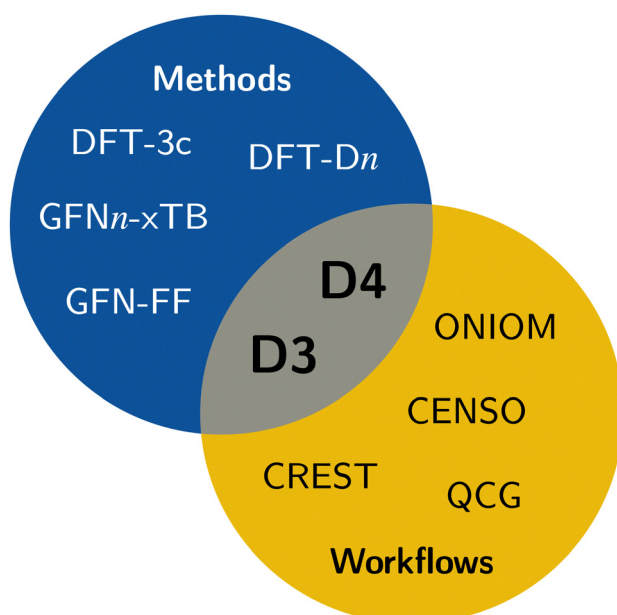


Fig. 1 Overview of typical applications of the D3 and D4 dispersion corrections.

2 Theory and implementation

2.1 Dispersion correction schemes

In most dispersion-corrected methods, including our D3 and D4 schemes, the total electronic energy consists of the energy



from the underlying mean-field approach and an additive contribution from the dispersion energy⁹⁴

$$E_{\text{total}} = E_{\text{MF}} + E_{\text{disp}} \quad (1)$$

The starting point of many dispersion correction methods is rooted in a second-order perturbation theory ansatz,^{95,96} which yields a pair-wise (two-body) dispersion energy.

$$E_{\text{disp}}^{(2)} = \sum_{n=6,8,\dots} E_{\text{disp},n}^{(2)} = - \sum_{n=6,8,\dots} \sum_{AB} \frac{C_n^{AB}}{R_{AB}^n} f_{\text{damp}}^{(n)}(R_{AB}) \quad (2)$$

The summation over n th-order energies originates from the multipole expansion of the Coulomb potential. R_{AB} denotes the internuclear distance of the atoms A and B in atom pair AB. The n th-order dispersion coefficients C_n^{AB} crucially define the accuracy of the method and their approximation is a central ingredient of each semi-classical dispersion correction. Finally, the damping function $f_{\text{damp}}^{(n)}(R)$ restricts the dispersion correction to the long-range regime, effectively removing the singularity and over-binding of eqn (2) for $R \rightarrow 0$ in the short-range regime.^{97,98} The lowest non-vanishing term ($n = 6$) relates to dipole-dipole interactions and dominates the asymptotic behavior with its R^{-6} decay. From a more practical perspective, the damping function can also avoid double counting of short-range dispersion effects that are sometimes already well described by the underlying mean-field method. By employing higher-order perturbation theory, the dispersion energy expression can be analogously extended beyond two-body terms.⁹⁹ However, many-body dispersion effects are often treated in a simpler, more approximate manner as they are typically much less important than two-body effects due to their small overall magnitude.^{100,101} Nonetheless, three-body terms can have a non-negligible effect when dealing with large, dense structures and are thus often additionally considered.

2.2 DFT-D3

The DFT-D3 approach extends and improves its predecessor DFT-D2,¹⁰² notably by explicitly considering the structural environment through the use of a so-called fractional coordination number CN. This adaptation recognizes that atoms in different bonding or hybridization states possess distinct coordination numbers, which aligns well with chemical intuition. A simplified flowchart of the DFT-D3 scheme is shown in Fig. 2.

To obtain the system-specific dispersion coefficients, reference dispersion coefficients $C_{6,\text{ref}}^{AB}(\text{CN}^A, \text{CN}^B)$ of the reference systems A_mH_n and B_kH_l are used. The values for m , n , k , and l are set individually for each reference system utilized. In principle, any realistic system can serve as a reference. For instance, structures such as P_2H_2 ($m = 2$, $n = 2$) or C_2H_4 ($m = 2$, $n = 4$) are already employed. These are pre-computed for every possible pair and obtained by a modified expression (eqn (4)) of the Casimir-Polder integration¹⁰³ (eqn (3)) of electric dipole polarizabilities at imaginary frequency $\alpha^A(i\omega^I)$ for many reference systems. In the following, $i\omega^I$ is used interchangeably with

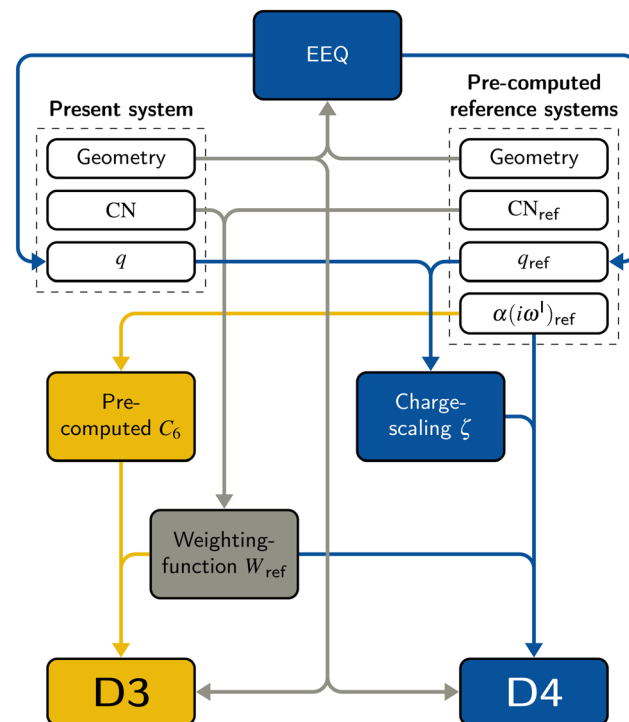


Fig. 2 Flow chart of the D3 and D4 models. White represents data that is either pre-computed or given by the input. Gray indicates parts that are used in both DFT-D3 and -D4 models. Yellow indicates the DFT-D3 model, blue the DFT-D4 model.

$i\omega$ for the imaginary part of $\omega = \omega^R + i\omega^I$.

$$C_6^{AB} = \frac{3}{\pi} \int_0^\infty \alpha^A(i\omega^I) \alpha^B(i\omega^I) d\omega \quad (3)$$

For the numerical integration, 23 values with $i\omega^I \in [1 \times 10^{-6}, 1 \times 10^1]$ are used.

$$C_{6,\text{ref}}^{AB}(\text{CN}^A, \text{CN}^B) = \frac{3}{\pi} \int_0^\infty \frac{1}{m} \left[\alpha^{A_m H_n}(i\omega^I) - \frac{n}{2} \alpha^{H_2}(i\omega^I) \right] \times \frac{1}{k} \left[\alpha^{B_k H_l}(i\omega^I) - \frac{l}{2} \alpha^{H_2}(i\omega^I) \right] d\omega \quad (4)$$

The dispersion coefficient of the actual D3 calculation $C_6^{AB}(\text{CN}^A, \text{CN}^B)$ for a specific atom pair AB is obtained by the Gaussian average of the pre-computed reference values weighted by the actual coordination number CN given by eqn (5).

$$\text{CN}^A = \sum_{B \neq A} \frac{1}{1 + \exp \left[-16 \left(\frac{4}{3} \frac{R_{A,\text{cov}} + R_{B,\text{cov}}}{R_{AB}} - 1 \right) \right]} \quad (5)$$

The DFT-D3 pair-wise dispersion energy is given by

$$E_{\text{disp}}^{\text{D3},AB} = - \sum_{AB} \sum_{n=6,8} s_n \frac{C_n^{AB}}{R_{AB}^n} f_{\text{damp}}^{(n)}(R_{AB}), \quad (6)$$

and is often extended by three-body dipole-dipole-dipole contributions with an Axilrod-Teller-Muto (ATM)^{104,105} term, as shown in eqn (13). The s_n coefficients are method-specific scaling parameters. While multiple variants of the damping



function $f_{\text{damp}}^{(n)}(R_{\text{AB}})$ have been proposed,^{106–108} we focus on the originally presented zero-damping¹⁵

$$f_{\text{zero}}^{(n)}(R_{\text{AB}}) = \frac{1}{1 + 6 \left(\frac{R_{\text{AB}}^{(n)}}{s_{r,n} R_0^{\text{AB}}} \right)^{a_n}}, \quad (7)$$

or the more frequently used Becke–Johnson (BJ) damping function^{24–26,97}

$$f_{\text{BJ}}^{(n)}(R_{\text{AB}}) = \frac{R_{\text{AB}}^{(n)}}{R_{\text{AB}}^{(n)} + (a_1 R_0^{\text{AB}} + a_2)^n}, \quad (8)$$

with $R_0^{\text{AB}} = \frac{C_{(8)}^{\text{AB}}}{C_{(6)}^{\text{AB}}}$, the pair-wise cutoff radius, which is interchangeably called van-der-Waals radius in this work. The zero-damping scheme uses fixed $a_6 = 14$ and $a_8 = 16$, and one method-specific parameter $s_{r,n}$, while BJ-damping utilizes the two method-specific parameters a_1 and a_2 .

2.3 DFT-D4

A simplified flowchart of the DFT-D4 scheme is shown in Fig. 2. The DFT-D4 model further improves DFT-D3 by introducing an atomic partial charge dependence of the atomic reference polarizabilities $\alpha^{\text{A}}(i\omega^{\text{I}})$ through the charge-scaling function $\zeta(z^{\text{A}}, z^{\text{A,ref}})$.

$$\zeta(z^{\text{A}}, z^{\text{A,ref}}) = \exp \left[\beta \left\{ 1 - \exp \left[\gamma^{\text{A}} \left(1 - \frac{z^{\text{A,ref}}}{z^{\text{A}}} \right) \right] \right\} \right] \quad (9)$$

Here, β is a global parameter and γ^{A} is the chemical hardness of A. The chemical hardness γ^{A} is a nonfitted element-specific parameter (second energy derivative w.r.t. change of electron number) to control the steepness of the scaling function and is taken from ref. 109. The atomic charge z^{A} is given as the sum of the nuclear charge Z^{A} and the atomic partial charge q^{A} . The charges q^{A} for the actual and reference systems are obtained *via* the classical electronegativity equilibration model (Section 2.4). The scaling is intended to increase the magnitude of the atomic dynamic polarizabilities for a larger number of electrons in proximity to the considered atom.

$$\alpha^{\text{A,ref}}(i\omega^{\text{I}}, z^{\text{A}}) = \alpha^{\text{A,ref}}(i\omega^{\text{I}}) \zeta(z^{\text{A}}, z^{\text{A,ref}}) \quad (10)$$

After the charge scaling, the geometry-based interpolation over the charge-scaled element-specific reference systems is done similarly to the fractional coordination number in DFT-D3 (eqn (5)), but now additionally considers an electronegativity difference dependence $\delta_{\text{AB}}^{\text{EN}}$ (eqn (11)) of the respective atom pair.

$$\delta_{\text{AB}}^{\text{EN}} = \frac{k_1 \exp[|\text{EN}_A - \text{EN}_B| + k_2]}{k_3} \quad (11)$$

Here, k_1 , k_2 , and k_3 are global parameters. The interpolation is

done *via* a weighting function $W_{\text{A}}^{\text{A,ref}}$,

$$\begin{aligned} & \alpha^{\text{A,ref}}(i\omega^{\text{I}}, z^{\text{A}}, \text{CN}^{\text{A}}) \\ &= \sum_{\text{A,ref}}^{N_{\text{A,ref}}} \alpha^{\text{A,ref}}(i\omega^{\text{I}}, z^{\text{A}}) W_{\text{A}}^{\text{A,ref}}(\text{CN}^{\text{A}}, \text{CN}^{\text{A,ref}}) \end{aligned} \quad (12)$$

determining the contribution of each reference value $\alpha^{\text{A,ref}}(i\omega^{\text{I}}, z^{\text{A}})$ to the final atom-in-molecule polarizability of atom A. These are used to calculate the pairwise dispersion coefficients C_6^{AB} *via* a numerical Casimir-Polder integration (eqn (3)) on the fly. With C_6^{AB} known, also C_8^{AB} (dipole–quadrupole coefficient) and C_9^{ABC} (triple–dipole coefficient) can be approximated.

The final energy expression of the DFT-D4 model is given by eqn (13).

$$\begin{aligned} E_{\text{disp}}^{\text{D4}} = & -\frac{1}{2} \sum_{\text{AB}} \sum_{n=6,8} s_n \frac{C_n^{\text{AB}}}{R_{\text{AB}}^{(n)}} f_{\text{BJ}}^{(n)}(R_{\text{AB}}) \\ & - \frac{1}{6} \sum_{\text{ABC}} s_9 \frac{C_9^{\text{ABC}}}{R_{\text{ABC}}^{(9)}} f_{\text{BJ}}^{(9)}(R_{\text{ABC}}, \theta_{\text{ABC}}) \end{aligned} \quad (13)$$

Here, θ_{ABC} is an angle-dependent term needed for the ATM three-body interaction, and s_6 and s_8 are method-specific parameters. Note that s_6 is usually set to unity to guarantee the correct behavior of the dispersion correction in the asymptotic limit.² D4 utilizes the Becke–Johnson (BJ) damping function (eqn (8)).

2.4 Electronegativity equilibration charges

The partial charges used in the polarizability scaling are obtained with the classical electronegativity equilibration charge (EEQ) model. It is based on electronegativity equilibration of Gaussian-type charge densities.¹¹⁰ This is done by minimizing the following isotropic electrostatic (IES) energy expression (eqn (14)) with respect to the atomic charges. In the following, the equations are given in matrix notation, where capital bold letters indicate matrices and non-capital bold letters vectors. The individual atomic partial charges q_{A} are the elements of the vector \mathbf{q} .

$$E_{\text{IES}} = \mathbf{q}^{\text{T}} \left(\frac{1}{2} \mathbf{A} \mathbf{q} - \mathbf{x} \right) \quad (14)$$

The elements of \mathbf{A} and \mathbf{x} are given by the following expressions.

$$\begin{aligned} x_{\text{A}} &= -\text{EN}_{\text{A}} + \kappa_{\text{A}} \sqrt{\text{mCN}_{\text{A}}} \\ A_{\text{AB}} &= \begin{cases} J_{\text{AA}} + \frac{2\gamma_{\text{AA}}}{\sqrt{\pi}} & \text{if } \text{A} = \text{B} \\ \frac{\text{erf}(\gamma_{\text{AB}} R_{\text{AB}})}{R_{\text{AB}}} & \text{if } \text{A} \neq \text{B} \end{cases} \\ \gamma_{\text{AB}} &= \frac{1}{\sqrt{a_{\text{A}}^2 + a_{\text{B}}^2}} \end{aligned}$$

For each element A, four parameters are used: electronegativity EN_{A} , hardness J_{AA} , coordination number scaling parameter κ_{A} , and width of Gaussian charge distribution a_{A} . These parameters are obtained by parameterization against accurate



reference charges (DFT Hirshfeld level) using a dataset as described in Section 4.3. To obtain EEQ partial charges from these equations, the method of constrained Lagrangian optimization is employed under the constraint that the sum of the partial charges conserves the total charge q_{total} of the system.

2.5 Dynamic purely imaginary-frequency polarizabilities

In order to evaluate the dispersion coefficients in eqn (3) and (4), the isotropic polarizabilities

$$\alpha = \frac{1}{3} \sum_{\alpha=x,y,z} \alpha_{\alpha\alpha} \quad (15)$$

with purely imaginary frequencies $i\omega^I$ are computed from the trace of the dipole polarizability tensor

$$\alpha_{\alpha\beta}(i\omega^I) = -\langle\langle \hat{\mu}_\alpha; \hat{\mu}_\beta \rangle\rangle_{\omega^I} \quad (16)$$

in the dipole length representation with the operators $\hat{\mu}_\alpha$. For self-consistent field (SCF) theories, the linear response function in eqn (16) is evaluated from the first electronic derivative of the dipole operator $\mathbf{V}^{[1]}$ and the second electronic derivative matrices $\mathbf{E}^{[2]}$ and $\mathbf{S}^{[2]}$ by

$$\langle\langle \hat{\mu}_\alpha; \hat{\mu}_\beta \rangle\rangle_{\omega^I} = -(\mathbf{V}^{[1]})_\alpha^\dagger (\mathbf{E}^{[2]} - (\omega^R + i\omega^I) \mathbf{S}^{[2]})^{-1} \mathbf{V}_\beta^{[1]}, \quad (17)$$

in which we consider only the purely imaginary part $i\omega^I$.¹¹¹ The real super matrices in eqn (17),

$$\mathbf{E}^{[2]} = \begin{pmatrix} \mathbf{A} & \mathbf{B} \\ \mathbf{B} & \mathbf{A} \end{pmatrix}, \quad \mathbf{S}^{[2]} = \begin{pmatrix} \Sigma & \Delta \\ -\Delta & -\Sigma \end{pmatrix}, \quad \mathbf{V}_\alpha^{[1]} = \begin{pmatrix} \mu_\alpha \\ -\mu_\alpha \end{pmatrix}, \quad (18)$$

exhibit a gerade (g) and ungerade (u) symmetry when being multiplied by symmetrized vectors.^{112–114} To avoid matrix inversion in eqn (17), the following linear response equations are solved iteratively for every imaginary frequency ω^I and Cartesian electric dipole operator component α .

$$\begin{pmatrix} -\mathbf{E}^{[2]} & \omega^I \mathbf{S}^{[2]} \\ \omega^I \mathbf{S}^{[2]} & \mathbf{E}^{[2]} \end{pmatrix} \begin{pmatrix} \mathbf{X}_g^I \\ \mathbf{X}_u^R \end{pmatrix} = -\begin{pmatrix} \mathbf{V}_g^I \\ -\mathbf{V}_u^R \end{pmatrix} \quad (19)$$

The frequency and operator component indices are omitted in eqn (19) for the sake of simplicity.

Alternatively, polarizabilities at purely imaginary frequencies can also be computed approximately by truncated moment expansions in order to avoid complex algebra.^{115–117} However, we have not introduced such approximations because the imaginary-frequency dynamic polarizabilities can be computed as efficiently as the ones with real frequencies without introducing any computational overhead.

The usage of purely-imaginary frequencies provides a powerful mathematical tool to simplify calculations and provide more stable numerical results. The usage of those was already shown to offer very accurate treatment of quantum many-body correlations,^{118–120} like dispersion-energy coefficients.¹²¹ They enable controllable simulation of equilibrium properties, nuclear quantum phenomena, and other non-adiabatic effects

– often disadvantages of *ab initio* methods like quantum Monte Carlo approaches.^{122–124}

3 Computational details

Quantum chemical calculations were performed with xtb 6.5.1, xtb-python 22.1, ORCA 5.0.4^{125,126} and the development version of ORCA 6.0. For calculations involving actinide elements, a locally-dense basis set approach is used for the actinide only. The def-TZVP¹²⁷ and ma-def-TZVP¹²⁸ basis for the actinides were used and implemented into the development version of ORCA 6.0. PBE0-NL/def2-SVP¹²⁹ (def-TZVP for the actinide) was generally employed for geometries. For the creation of the hydride reference structures, PBE0/def2-TZVP (def-TZVP for the actinide) was used. Hirshfeld population analysis¹³⁰ single points were calculated using ωB97M-V/def2-TZVPP¹³¹ (ma-def-TZVP for the actinide). The final benchmarking studies use *DefGrid3* grid, geometries were obtained using def2-TZVP (ma-def-TZVP for the actinide) and single-point energies are calculated using ma-def2-TZVP basis (ma-def-TZVP for the actinide). Matching general-purpose auxiliary basis sets were automatically constructed on the fly using ORCA's *AutoAux*.¹³² The *RJJCOSX*^{133–135} approximation was used for all calculations. The *DefGrid2* option was applied for the numerical integration grid as well as *TightSCF* convergence criteria as implemented in ORCA. For all calculations, the matching def2 (def for the actinide) effective small core potentials (ECPs)^{127,128,136,137} for heavy elements with $Z > 36$ were generally employed. The matching ECPs for the actinides already account for relativistic effects. The quality of the ECPs was tested against scalar relativistic, all-electron (ZORA) calculations for the geometries and dynamic purely-imaginary frequency polarizabilities and provide very similar results. These results for the actinium hydrides can be found in the ESI.†

The SCF frequency-dependent polarizabilities were implemented into the development version of ORCA 6.0. For the calculation of the frequency-dependent polarizabilities of the reference systems, unrestricted PBE38/ma-def2-TZVP¹³⁸ was used with tight convergence criteria (*TightSCF*) and *DefGrid3* grid. PBE38 was chosen due to its robustness and successful application in previous parameterizations of the DFT-D dispersion corrections.^{15,139} This also ensures the greatest possible consistency with the existing parameterization of other elements. For every system, 23 frequency-dependent polarizabilities were calculated between $i\omega_{\min}^I = 10^{-6}$ and $i\omega_{\max}^I = 10.0$.

DFT-NL was calculated using the ORCA native, non-self-consistent, post-SCF implementation. DFT-D3 and -D4 dispersion corrections were calculated using development versions of simple-dftd3 1.0.0 and dftd4 3.6.0, as well as the development version of ORCA 6.0.

All new functionalities implemented in the development version of ORCA will be made available in the upcoming version of ORCA 6.0.



4 Parameterization

This chapter is divided into parameterization of DFT-D3 and DFT-D4 for a better overview, although some parameters are used in both models.

4.1 Parameterization of DFT-D3

4.1.1 $\frac{\langle r_A^4 \rangle}{\langle r_A^2 \rangle}$ Expectation values. The ratio of $\frac{\langle r_A^4 \rangle}{\langle r_A^2 \rangle}$ is used for the recursive calculation of the pairwise dipole-quadrupole C_8^{AB} dispersion coefficients. The individual expectation values at the four-component relativistic PBE/Dyall-AE4Z^{140–142} levels of theory were used as provided in the framework of D3 parameterizations of super heavy elements.^{143–145} The respective $\frac{\langle r_A^4 \rangle}{\langle r_A^2 \rangle}$ expectation values can be found in Section B.2 of the ESI.[†]

4.1.2 Covalent radii. The covalent radii used for the calculation of the fractional coordination number and taken from ref. 146 and can be found in Section B.3 of the ESI.[†]

4.1.3 Van-der-Waals radii. The values were originally derived from the distance for which the first-order DFT interaction energy between the atoms A and B equals a cutoff energy. However, this approach yielded faulty results for some of the atom pairs involving actinides, likely due to the presence of strong static correlation effects. Instead, the van-der-Waals radius of an atom pair was derived by multiplying the sum of their respective covalent radii by 0.7. The atom pair-wise van-der-Waals radii can be found in Section B.4 of the ESI.[†]

4.1.4 C_6^{AB} coefficients. The pair-wise C_6^{AB} coefficients were obtained using the dynamic purely-imaginary frequency polarizabilities as obtained in Section 4.2 using the modified Casimir-Polder expression (eqn (4)).

4.2 Parameterization of DFT-D4

4.2.1 Chemical hardnesses. The element-specific chemical hardnesses for the charge scaling function used to extrapolate the C_6 coefficients in DFT-D4 are taken from ref. 109 and can be found in Section C.1 of the ESI.[†]

4.2.2 Electronegativities. Pauling electronegativities are used for the improved fractional coordination number in D4. These are taken from ref. 147; electronegativities for the elements U, Np, and Pu are taken from ref. 148. The electronegativity for Lr was assigned to a value of 1.3 to maintain consistency with the preceding transplutonium elements.^{149–151} The Pauling electronegativities can be found in Section C.2 of the ESI.[†]

4.2.3 Dynamic purely-imaginary frequency polarizabilities. Generally, all hydrides of the form AH_n with $n = \{0, 1, 2, 3, 4, 5, 6\}$ are used, however, a few systems were discarded due to convergence issues. For a complete list and details about the used reference systems, see the ESI.[†]

The dynamic purely-imaginary frequency polarizabilities were obtained as described in Section 3. For D3, the described modified Casimir-Polder expression (eqn (4)) was used to obtain the atom pair-wise dispersion coefficients C_6^{AB} . Both, the dynamic purely-imaginary frequency polarizabilities and

the atom pair-wise parameters can be found in Section C.4 of the ESI.[†]

4.2.4 Reference coordination number and charges. The reference coordination numbers are obtained in line with their definition in the D3 and D4 models, respectively. The reference charges of the reference systems are obtained with the EEQ model. The parameterization of the EEQ model is described in the next section. Both the coordination numbers and the reference EEQ charges for all reference systems can be found in Section C.4 of the ESI.[†]

4.3 Parameterization of EEQ

For the parameterization of the EEQ model, a set of actinide structures called AcQM was created. The set contains in total 2537 structures. The first part of 1283 structures contain realistic actinide complexes that were created using the Architect^{152,153} combined with our ArchitectWrapper package,¹⁵⁴ as described in our recent LnQM set.¹⁵⁵ The structures were generated with only stable oxidation states of the central actinide with coordination numbers ranging from four to 10. The second part contains 1254 structures of smaller hydrides, fluorides, chlorides, oxides, and sulfides as well as various mindless structures. Mindless structures are randomly generated artificial molecules, that extend the structural space beyond conventional chemical intuition and thus including much more diverse structures. This helps to make the parameterization and model more robust. These structures were created by a program that randomly places 1–8 atoms from the first five periods of the periodic table (excluding any transition metals) together with a single actinide in close vicinity to each other. This procedure is described in detail in ref. 156; additionally, some examples are given in the ESI.[†] A first crude optimization of the structures using the respective lanthanide homolog was done using GFN2-xTB, followed by the described (Section 3) DFT geometry optimization. The AcQM set with the PBE0-NL optimized structures and the ω B97M-V Hirshfeld partial charges is provided in the ESI,[†] and on GitHub at github.com/grimme-lab/acqm.

The EEQ model was parameterized against the obtained Hirshfeld charges using a modified simplex algorithm^{157,158} with the loss function given in the ESI.[†] Here, only the systems with total charges ranging from -1 to $+1$ are used to ensure the reliability of the reference Hirshfeld charges. The obtained parameters are given in Section D.3 of the ESI.[†]

The parameterization yields a mean absolute error (MAE) of $0.21e^-$ and a root mean squared error (RMSE) of $0.25e^-$ for all actinide charges of the AcQM set against the reference Hirshfeld charges (Fig. 3).

5 Results and discussion

We tested the extension of the D3 and D4 models through multiple case studies focusing on various actinide compounds. As only the DFT-D4 extension is implemented in ORCA, the geometries are only tested with D4. With this, we aim to



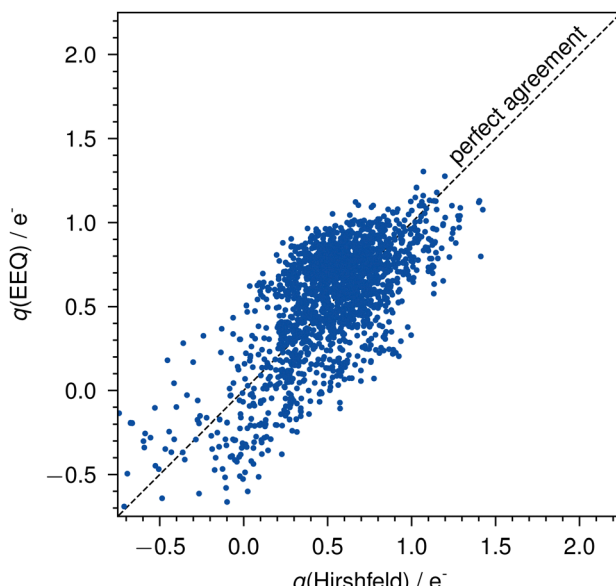


Fig. 3 Errors of the EEQ model against Hirshfeld charges on the AcQM set. The dashed line indicates perfect agreement.

qualitatively assess the performance, especially to show the relative effect of utilizing dispersion correction schemes, while using experimental data as a reference where applicable. An in-depth quantitative analysis is not our goal and also not feasible due to a lack of experimental and, above all, accurate theoretical reference data. Studies investigating the general performance of dispersion corrections can be found in, *e.g.*, ref. 29 and 159–162.

Additionally, the density-dependent non-local dispersion correction DFT-NL will also be evaluated as a comparison. Generally, D3 and NL are found to perform similarly,^{161,163} However, NL sometimes offers an advantage when it comes to metallic systems where the electronic structure changes significantly – such as in ionization reactions.¹⁶⁴ D4 seems to be able to keep up with NL in most cases and may offer better performance for general thermochemistry and larger systems compared to NL.^{33,161,165}

NL requires reasonably accurate electron densities to obtain good results, which requires an expensive converged SCF density from, *e.g.*, density functional theory. This means that the addition of NL in retrospect is not possible if no electron density is saved, and thus, requires the calculation to be redone. It is important to note that NL only includes dipole-dipole interactions (C_6) and no dipole-quadrupole (C_8) or many-body effects (*e.g.*, C_9). The DFT-NL implementation in ORCA uses the non-local part of the VV10 functional,²⁰ which requires a functional specific parameter b . This parameter can be obtained from parameterization on non-covalent interaction (NCI) benchmark sets like the NCIBLIND10,¹⁶⁶ S66 \times 8^{167–169} and S22 \times 5.^{170,171} The parameterization of b can in principle absorb some of the missing higher-order interactions but could also lead to overestimated dipole-dipole contributions.^{172,173}

For the following test calculations, the common B3LYP^{174,175} and PBE0 functionals are used.

5.1 Dissociation curves

Dissociation curves for actinium³⁺ with argon, and for neutral nobelium with neon are calculated using B3LYP, without dispersion correction, with NL, D3, and D4. The Ac³⁺–Ar dissociation curve is shown in Fig. 4, the No–Ne dissociation curve is shown in Fig. 5.

For the threefold positive actinide ion, both D4 and NL yield very similar dispersion energies. In contrast, D3 tends to slightly over-bind in this case when compared to D4 and NL.

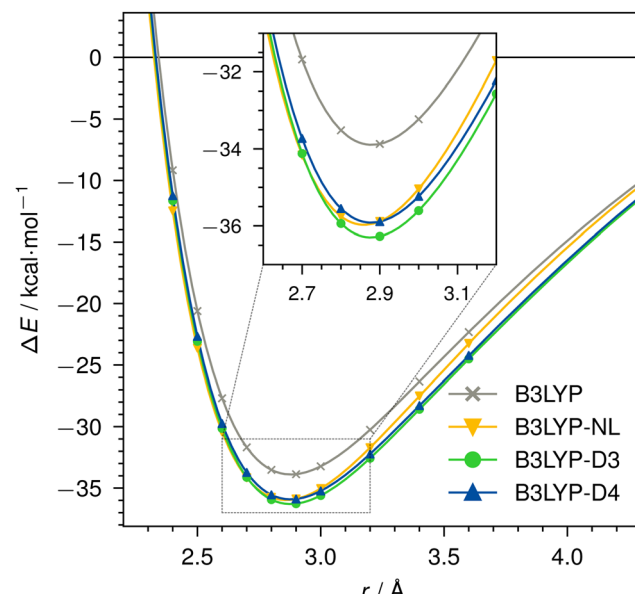


Fig. 4 Dissociation curve of Ac³⁺–Ar for B3LYP/def2-TZVP without dispersion correction, with NL, D3, or D4.

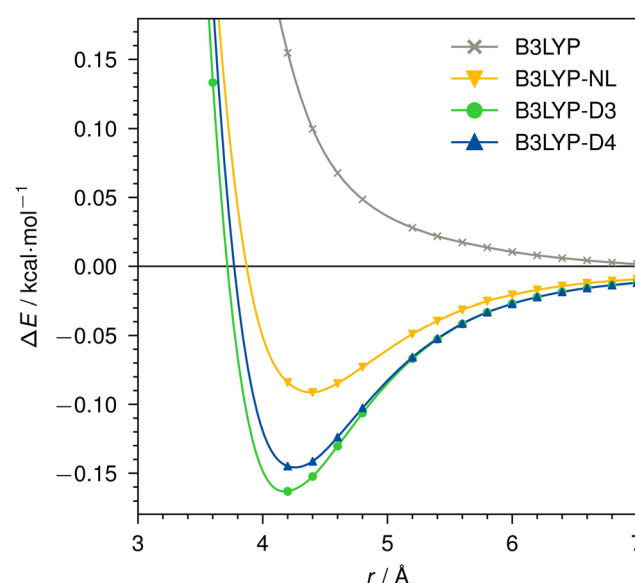


Fig. 5 Dissociation curve of No–Ne for B3LYP/def2-TZVP without dispersion correction, with NL, D3, or D4.



Table 1 Equilibrium bond distances between uranium and chlorine/fluorine for various complexes for different methods against experimental reference in Å

Bond	Structure	Exp.	B3LYP			PBE0		
			—	NL	D4	—	NL	D4
U–F	UF ₆	1.999, 1.997 ^{177,178}	2.007	2.002	2.007	1.989	1.986	1.988
	UF ₅	—	2.027	2.021	2.026	2.009	2.006	2.009
	UF ₄	—	2.065	2.058	2.064	2.048	2.046	2.048
	UF ₃	—	2.071	2.061	2.070	2.060	2.057	2.058
U–Cl	UCl ₆	2.420, 2.461 ¹⁷⁹	2.469	2.456	2.464	2.436	2.430	2.434
	UCl ₅	—	2.484	2.472	2.479	2.454	2.448	2.453
	UCl ₄	—	2.508	2.496	2.504	2.482	2.476	2.480
	UCl ₃	2.549 ¹⁸⁰	2.553	2.536	2.548	2.412	2.393	2.404

This is expected due to the missing charge dependency of D3, which D4 incorporates. This decreases the dynamic atomic polarizabilities and, thus, the C_n coefficients, particularly, in cases with fewer electrons compared to the neutral state. The density dependency of NL inherently accounts for this atomic charge dependency. Even though the NL correction can be prone to under-bind simple diatomic cases due to the missing higher-order contributions,¹ we find excellent agreement in this instance. The minimum of the Ac^{3+} –Ar dimer is identical for all cases, as the interaction energy is comparably large and already well described by the density functional itself. The missing dispersion contribution plays only a minor role.

For the neutral No–Ne case, no attractive interaction is found without applying a dispersion correction. This behavior is analogous to, *e.g.*, the Kr–Kr dimer shown in ref. 95. With dispersion correction, the interaction of the two atoms is correctly predicted as attractive and shows the expected behavior of a vdW dimer. While we find very similar result for D3 and D4, NL provides a noticeably less attractive dispersion interaction. For B3LYP in the No–Ne case, the total dispersion contribution at 2.2 Å is $-0.6 \text{ kcal mol}^{-1}$, of which $-0.2 \text{ kcal mol}^{-1}$ is due to dipole–dipole (C_6) and $-0.4 \text{ kcal mol}^{-1}$ due to dipole–quadrupole (C_8) interaction. The bond-distance minimum of the dimer is identical with D3 and D4, NL however predicts a 0.2 Å longer bond.

5.2 Uranium molecular compounds

Uranium halogenide compounds of the type UX_n with $\text{X} = \{\text{F}, \text{Cl}\}$ and $n = \{3, 4, 5, 6\}$ are used to evaluate bond distances.¹⁷⁶ The resulting bond distances with the experimental reference can be found in Table 1.

Unsurprisingly, U–F distances are hardly changed by using D4, compared to plain B3LYP or PBE0. The covalent bonds are already well described by the semi-local correlation functionals. For cases, where the dispersion is already well covered by the density functional, we find no deterioration of performance upon using D4 dispersion correction and the equilibrium bond distances mainly depend on the employed density functional. The short-range damping function of the non-local NL correction does not damp covalent bonds entirely and thus predicts slightly smaller bond distances compared to D4, for all U–F distances. For the longer U–Cl distances, the D4 damping

function allows small amounts of dispersion interactions and thus leads to slightly smaller covalent bonds upon employing D4. However, the majority of the dispersion contribution is due to dispersion interactions between the Cl ligands. For UCl₆, the total D4 dispersion contribution is $-19.0 \text{ kcal mol}^{-1}$, of which $-10.3 \text{ kcal mol}^{-1}$ is only due to the Cl–Cl pair-wise dispersion interactions. This can be analyzed by using DFT-D4's feature to calculate a pairwise decomposition of the dispersion energy. For DFT-NL, the same as with U–F is observed: NL predicts a stronger dispersion interaction compared to D4 and thus yields smaller bond distances.

5.3 Crystal structures

As a further test, a systematic investigation of geometries was carried out using molecular crystal cutouts. The structures were obtained from the Cambridge Structural Database (CSD).¹⁸¹ The unit cell of the respective crystals was used to create a cluster of molecules. We mainly used cases where the 5f subshell is either fully empty, fully singly, or fully doubly occupied (*i.e.*, 5f⁰, 5f⁷, or 5f¹⁴), as otherwise larger amounts of static correlation effects may be present.¹⁸²

Each structure was optimized using B3LYP and PBE0 with each no dispersion correction, D4, or NL dispersion

Table 2 Heavy-atom best-fit RMSD of the obtained geometries compared to the experimental structures for various CSD molecular crystal structure cutouts in Å. B3LYP and PBE0 with each no dispersion correction, D4, and NL dispersion corrections are shown

CCSD-ID	Formula	B3LYP			PBE0		
		—	NL	D4	—	NL	D4
1047312 ^{184,185}	$\text{ThC}_{21}\text{H}_{28}\text{Si}_2$	0.29	0.03	0.15	0.41	0.03	0.14
1100351 ¹⁸⁶	$\text{NpC}_{20}\text{H}_{28}\text{O}_8$	0.29	0.39	0.08	0.93	0.32	0.78
1100378 ¹⁸⁷	$\text{UC}_{10}\text{H}_{14}\text{O}_7$	0.46	0.27	0.28	0.45	0.27	0.28
1100552 ¹⁸⁸	$\text{UC}_{15}\text{H}_{21}\text{O}_8$	0.23	0.34	0.35	0.24	0.28	0.31
1553027 ^{189,190}	$\text{U}_{2}\text{C}_{30}\text{H}_{26}\text{O}_6\text{N}_4\text{Cl}_4$	0.75	0.73	0.70	0.70	0.66	0.64
1554548 ^{191,192}	$\text{ThC}_{32}\text{H}_{37}\text{N}_4\text{Cl}$	0.15	0.07	0.08	0.13	0.07	0.07
1554554 ^{193,194}	$\text{ThC}_{46}\text{H}_{56}\text{O}_2\text{N}_4$	0.29	0.32	0.30	0.21	0.30	0.29
1557708 ^{195,196}	$\text{AmC}_{16}\text{H}_{32}\text{O}_4\text{Br}_3$	0.51	0.46	0.48	0.53	0.48	0.49
1841778 ^{197,198}	$\text{AmC}_{27}\text{H}_{38}\text{S}_6\text{N}_5$	0.67	0.47	0.49	0.65	0.50	0.49
2168159 ^{199,200}	$\text{CmO}_{18}\text{N}_6$	0.32	0.27	0.30	0.28	0.26	0.28
713927 ^{201–203}	$\text{Uc}_6\text{O}_8\text{H}_9$	0.14	0.13	0.13	0.13	0.13	0.13
726784 ^{204,205}	$\text{NpC}_{13}\text{H}_{15}\text{O}_5\text{N}_2$	0.24	0.22	0.27	0.23	0.35	0.26
793245 ^{206,207}	$\text{UC}_{16}\text{H}_{21}\text{O}_6\text{N}$	0.33	0.33	0.26	0.33	0.33	0.32
Mean		0.37	0.34	0.33	0.41	0.34	0.36



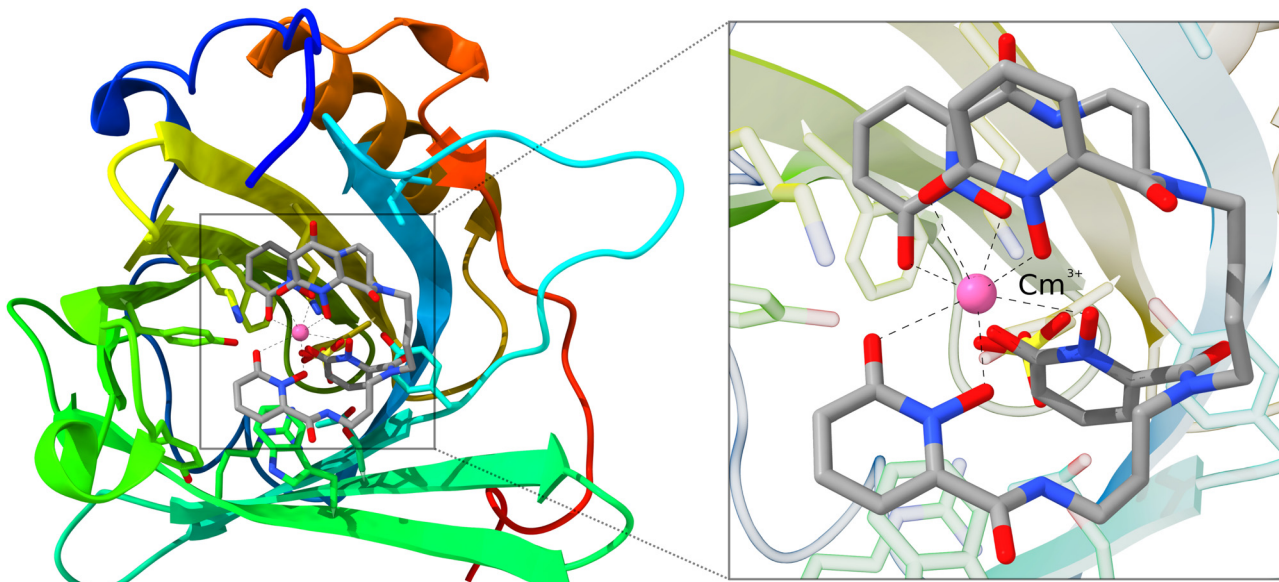


Fig. 6 Structure of the Cm^{3+} -siderocalin complex; the inner Cm^{3+} -4OL is highlighted and enlarged on the right. Hydrogen atoms are hidden for better visibility.

corrections. The heavy-atom best-fit RMSD (hRMSD) of the obtained geometries compared to the experimental structures was calculated using quaternions.¹⁸³ The resulting hRMSD in Å are given in Table 2. A value below 0.40 Å can be considered as a very good agreement for such large structures.

The mean hRMSD for both functionals improves by using the D4 or NL dispersion correction. B3LYP-D4 is found to perform slightly better than its NL counterpart; PBE0-D4 and -NL deliver very similar results.

D4 improves almost every structure compared to B3LYP. The single exception (1100552) still exhibits a good hRMSD of 0.35 Å. D4 is also found to systematically improve the geometries of plain PBE0, only two structures (1100552 and 1554554) are slightly worse with PBE0-D4 compared to uncorrected PBE0.

5.4 Bioorganic complex

As mentioned in the introduction, QM/MM schemes are a popular choice for treating large structures, especially for biochemical modeling. With those schemes, the structure of interest is partitioned into two regions that are treated with different methods. The more important part is calculated using a higher-level, more expensive method. As a demonstration, we use the inner Cm^{3+} -4OL[§]-complex of a large siderocalin complex (4ZHF)^{208,209} as a cutout. The inner complex is used unchanged and does not require any cutting and capping of chemical bonds, as the complex is an individual molecule that is bound non-covalently to the protein. This structure was obtained from the protein data bank (PDB).^{210,211} The complex is shown in Fig. 6.

[§] N,N'-butane-1,4-diylbis[1-hydroxy-N-(3-[(1-hydroxy-6-oxo-1,6-dihydropyridin-2-yl)carbonyl]aminopropyl)-6-oxo-1,6-dihydropyridine-2-carboxamide]

This cutout is optimized with plain B3LYP, combined with D4, and NL. The calculations with PBE0 could not be converged. The optimized bond distances between Cm^{3+} and the oxygens of the 4OL ligand, as well as the intermolecular distance of the benzene moieties of the 4OL ligand are given in Table 3; an overlay of the resulting optimized structures is shown in Fig. 7. The bond distances between the central Cm^{3+} and the oxygens of the 4OL ligand are found to be systematically smaller by employing NL or D4 dispersion corrections. The distances between the benzene moieties of the 4OL ligand are also smaller by employing NL or D4 dispersion corrections. This can also be seen in the overlay of the optimized structures in Fig. 7. In addition, the anisotropy in the distance between the two pairs of ring moieties is lost with any of the calculated geometries compared to the experimental crystal structure.

Compared to the crystallographic results of Allred *et al.*, we find too small mean bond distances by B3LYP-D4 or -NL. The distance between the left ring moieties improves upon employing a dispersion correction, whereas the right ring moieties become too small. The used cutout is a rough approximation, as the surrounding protein is not incorporated at all. This is also the reason for the missing anisotropy in the distance between the two pairs of ring moieties which could also be

Table 3 Mean bond distances of Cm^{3+} -4OL complex in Å. Experimental reference is taken from ref. 208. The ring moieties are denoted as shown in Fig. 7

Bond	Exp.	B3LYP		
		—	NL	D4
$\text{Cm}^{3+}\text{--O}^{(1-6)}$	2.539	2.469	2.441	2.447
$\text{H}_6\text{C}_6\text{--C}_6\text{H}_6$ (left)	5.281	6.254	5.555	5.163
$\text{H}_6\text{C}_6\text{--C}_6\text{H}_6$ (right)	7.090	6.253	5.588	5.138



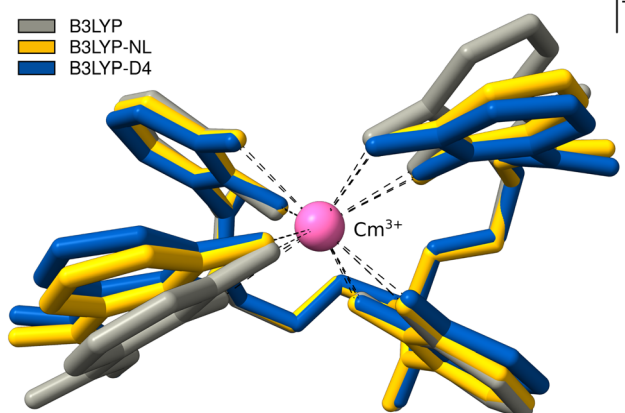


Fig. 7 PBE0-D4/def2-SVP Optimized structures of Cm^{3+} -4OL with B3LYP, B3LYP-NL, and B3LYP-D4. Hydrogen atoms are omitted for clarity.

caused by crystal packing in the experimental X-ray structure. The missing description of dispersion interactions offers good error compensation in this case for the mean distance between the two pairs of ring moieties, which is the reason why the agreement with the experiment worsens upon employing a dispersion correction, however, the anisotropy is still lost. The inclusion of the protein will likely slightly increase the Cm^{3+} -4OL and $\text{H}_6\text{C}_6\text{--C}_6\text{H}_6$ distances and could also introduce the anisotropy due to attractive dispersion interactions with the surrounding protein. Given the current lack of advanced semi-empirical methods tailored for actinides, implementing a QM/MM-type scheme is not straightforward and would require substantial effort. Our tests on crystal structures indicate that dispersion corrections typically enhance accuracy considerably. Consequently, we expect similar improvements in this case when a comprehensive description of the entire structure is employed.

5.5 Role of actinide dispersion interaction

For many transition metal complexes and clusters, it is crucial to have a robust description of metal–non-metal dispersion to correctly model those systems.²¹² This is, for example, the case for transition metal–alkane interactions in σ -complexes,²¹³ or in the formation of the Grubbs II catalyst.²¹⁴ However, the metal–metal dispersion interaction can also be important. This was found for gold nanoparticles,²¹⁵ zinc, cadmium, and mercury clusters,²¹⁶ for interactions of metals and clusters with surfaces²¹⁷ or for the description of adsorption processes on metal surfaces^{218,219} or in bulk metal crystals.^{220,221} To show that this is also the case for the actinides, we provide examples where dispersion interactions involving actinides, either actinide–non-actinide or actinide–actinide, are significant and must be taken into account.

The actinide–actinide dispersion interaction is evaluated using a nobelium cluster consisting of 14 nobelium atoms, which is optimized using PBE0/def2-SVP with D4, NL, and without any dispersion correction. Nobelium offers the advantage of an electronically simple $7s^2\ 5f^{14}$ closed-shell

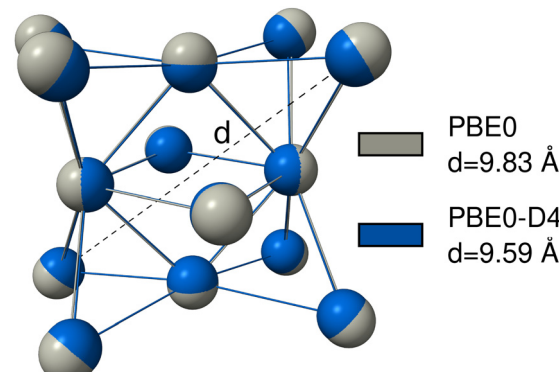


Fig. 8 PBE0/def2-SVP (grey) and PBE0-D4/def2-SVP (blue) optimized No_{14} -cluster. PBE0-NL/def2-SVP is hidden for better visibility, however, the result is very similar to the D4 result with $d = 9.55$ Å. The calculated diagonal distance is shown as the dashed black line.

configuration. To quantify the results, the cluster and its cross-diagonal distance, as shown in Fig. 8, is calculated with PBE0, PBE0-D4, and PBE0-NL. The non-dispersion corrected geometry yields the largest distance of $d = 9.83$ Å, while the D4 and NL geometries yield a very similar result with $d = 9.59$ Å and $d = 9.55$ Å, respectively.

The actinide–non-actinide dispersion interaction is investigated using diuranium carbide U_2C inside a $I_h(7)\text{-C}_{80}$ fullerene cage, which was recently experimentally stabilized by Zhang *et al.*²²² The $\text{U}_2\text{C}@\text{C}_{80}$ cluster is shown in Fig. 9. For this, the respective interaction energy of the process $\text{U}_2\text{C} + \text{C}_{80} \rightarrow \text{U}_2\text{C}@\text{C}_{80}$ is calculated. We find an interaction energy of -244.3 kcal mol⁻¹ for PBE0/ma-def2-TZVP, -292.3 kcal mol⁻¹ with NL, and -277.1 kcal mol⁻¹ with D4; -175.7 , -250.7 , and -232.8 kcal mol⁻¹ were found for the respective B3LYP/ma-def2-TZVP analogues. In all cases, the dispersion contribution is substantial, exceeding -33 kcal mol⁻¹ and accounting for more than 10% (up to 30% for B3LYP-NL) of the total interaction energy. NL yields a slightly larger dispersion contribution compared to D4, which could potentially originate from the missing many-body term in NL. The dispersion

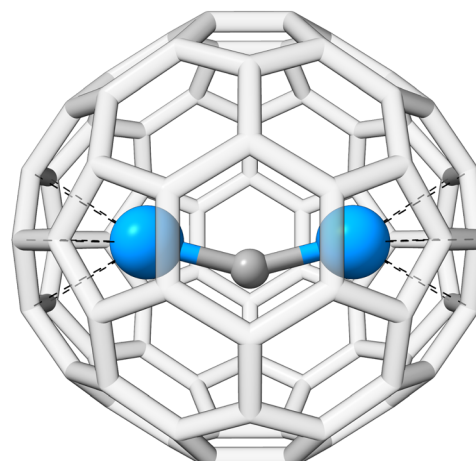


Fig. 9 PBE0-D4/def2-SVP optimized geometry of the $\text{U}_2\text{C}@\text{C}_{80}$ -cluster.



contribution to the interaction energy of DFT-D4 reveals that 80% stem from the $U_{U_2C}-C_{80}$ interaction, while only the remaining 20% arise from to $C_{U_2C}-C_{80}$ interaction.

6 Conclusions

Generally applicable and efficient dispersion corrections are an indispensable and integral part of various contemporary quantum chemical methods. Nevertheless, many heavy elements like actinides were barely considered during the development of efficient methods. This stands in stark contrast to the rich and diverse chemistry of the actinides, which holds significant importance across various domains of chemical research. As a consequence, the prominent D3 and D4 dispersion corrections lacked a complete and consistent parameterization for the actinides. In this work, we extended the D3 and D4 London dispersion corrections to the full actinides series, francium, and radium. To keep intrinsic consistency with the existing version for the rest of the periodic table, the original parameterization strategy of the D4 model was only slightly modified. Accordingly, reference Hirshfeld atomic partial charges were generated at the sophisticated ω B97M-V/ma-def-TZVP level to fit the required electronegativity equilibration charge model that is a key component of the D4 model. To facilitate this, a new actinide data set called AcQM was created that covers the most common chemical compound space of molecular actinide chemistry. The new parameter set was assessed for the computation of various dissociation curves of actinide atoms and ions, geometry optimizations of experimentally determined crystal structure cutouts and gas-phase structures of small uranium compounds, and an example extracted from a small actinide complex protein assembly. We find that the novel parameterizations perform on par with the computationally more demanding density-dependent NL variant of the VV10 dispersion correction for both geometric and energetic properties. On the other hand, in agreement with the literature on transition metals, we find that the actinide–actinide and actinide–non-actinide dispersion interaction can play an important role in many relevant actinide systems. With the presented extension to the actinides, the excellent cost-accuracy ratio of the D3 and D4 models can now be utilized to improve the accuracy of density functional, semi-empirical quantum mechanical, and force field methods for the description of actinide complexes. Without this extension, a robust description of the actinide chemical space would not be possible due to many relevant cases that require a good description of dispersion interactions. This development also facilitates the incorporation of efficient composite DFT methods, such as r^2 SCAN-3c, previously applied to other elements, into actinide research. These fast methods are crucial for investigating large actinide complexes, particularly, in the framework of QM/MM techniques. Moreover, they expedite the adaptation of established computationally demanding workflows and tasks, like conformer generation and high-throughput transition state sampling, to the field of actinide chemistry.

All extensions presented in this work are implemented in our freely available standalone codes, and the DFT-D4 parameterization as well as the efficient algorithm to compute dynamic polarizabilities will be available in the upcoming ORCA 6.0 program package.

Author contributions

Conceptualization: L. W., S. G., A. H. and M. B.; data curation: L. W., I. G. and M. F.; formal analysis: L. W., I. G. and M. F.; funding acquisition: S. G., A. H. and M. B.; investigation: L. W., I. G. and M. F.; methodology: S. G., A. H. and M. B.; project administration: A. H. and M. B.; resources: L. W., I. G., M. F., B. H.-P., S. G., A. H. and M. B.; software: L. W., I. G., M. F. and B. H.-P.; supervision: S. G., A. H. and M. B.; validation: L. W., I. G., M. F., B. H.-P., S. G., A. H. and M. B.; visualization: L. W.; writing – original draft: L. W., I. G., M. F. and B. H.-P.; writing – review & editing: L. W., I. G., M. F., B. H.-P., S. G., A. H. and M. B.

Data availability

All obtained parameters for the presented DFT-D3 and -D4 extensions, the parameters for the EEQ model, and the investigation of relativistic effects have been included as part of the ESI.† The full AcQM set is additionally included as part of the ESI,† but can also be found on GitHub at github.com/grimme-lab/acqm.

Conflicts of interest

M. B., B. H.-P. and S. G. are affiliated with the FACCTs GmbH which licenses the ORCA program package for commercial use.

Acknowledgements

The German Science Foundation (DFG) is gratefully acknowledged for financial support of S. G. Further, S. G. and M. B. gratefully acknowledge financial support from the Max Planck Society through the Max Planck fellow program. The authors would like to sincerely thank the University of Bonn for granting access to the Marvin Computing Cluster. The authors would also like to thank Jan-Michael Mewes, Christian Hölzer and Thomas Froitzheim for fruitful discussions. Open Access funding provided by the Max Planck Society.

Notes and references

- 1 S. Grimme, A. Hansen, J. G. Brandenburg and C. Bannwarth, *Chem. Rev.*, 2016, **116**, 5105–5154.
- 2 R. Eisenschitz and F. London, *Z. Phys.*, 1930, **60**, 491–527.
- 3 J. P. Wagner and P. R. Schreiner, *Angew. Chem., Int. Ed.*, 2015, **54**, 12274–12296.
- 4 J. N. Israelachvili, *Intermolecular and Surface Forces*, Elsevier, 2011, pp. 577–616.



5 J. Brandenburg, J. Bates, A. Ruzsinszky, J. Sun and J. Perdew, *Abstracts of Papers of the American Chemical Society*, 2016.

6 S. Grimme, F. Böhle, A. Hansen, P. Pracht, S. Spicher and M. Stahn, *J. Phys. Chem. A*, 2021, **125**, 4039–4054.

7 L. Goerigk, *Non-Covalent Interactions in Quantum Chemistry and Physics*, Elsevier, 2017, pp. 195–219.

8 L. Goerigk, A. Hansen, C. Bauer, S. Ehrlich, A. Najibi and S. Grimme, *Phys. Chem. Chem. Phys.*, 2017, **19**, 32184–32215.

9 N. Mardirossian and M. Head-Gordon, *Mol. Phys.*, 2017, **115**, 2315–2372.

10 S. Yoo and S. S. Xantheas, *J. Chem. Phys.*, 2011, **134**, 121105.

11 K. E. Riley and P. Hobza, *J. Chem. Theory Comput.*, 2008, **4**, 232–242.

12 Z. Ma, Y. Zhang and M. E. Tuckerman, *J. Chem. Phys.*, 2012, **137**, 044506.

13 A. S. Christensen, T. Kubáč, Q. Cui and M. Elstner, *Chem. Rev.*, 2016, **116**, 5301–5337.

14 S. Spicher and S. Grimme, *Angew. Chem., Int. Ed.*, 2020, **59**, 15665–15673.

15 S. Grimme, J. Antony, S. Ehrlich and H. Krieg, *J. Chem. Phys.*, 2010, **132**, 154104.

16 S. Grimme, S. Ehrlich and L. Goerigk, *J. Comput. Chem.*, 2011, **32**, 1456–1465.

17 E. Caldeweyher, C. Bannwarth and S. Grimme, *J. Chem. Phys.*, 2017, **147**, 034112.

18 E. Caldeweyher, S. Ehlert, A. Hansen, H. Neugebauer, S. Spicher, C. Bannwarth and S. Grimme, *J. Chem. Phys.*, 2019, **150**, 154122.

19 E. Caldeweyher, J.-M. Mewes, S. Ehlert and S. Grimme, *Phys. Chem. Chem. Phys.*, 2020, **22**, 8499–8512.

20 O. A. Vydrov and T. Van Voorhis, *J. Chem. Phys.*, 2010, **133**, 244103.

21 R. Sabatini, T. Gorni and S. De Gironcoli, *Phys. Rev. B: Condens. Matter Mater. Phys.*, 2013, **87**, 041108.

22 O. A. Vydrov and T. Van Voorhis, *Phys. Rev. Lett.*, 2009, **103**, 063004.

23 W. Hujo and S. Grimme, *J. Chem. Theory Comput.*, 2011, **7**, 3866–3871.

24 A. D. Becke and E. R. Johnson, *J. Chem. Phys.*, 2005, **123**, 154101.

25 E. R. Johnson and A. D. Becke, *J. Chem. Phys.*, 2005, **123**, 024101.

26 E. R. Johnson and A. D. Becke, *J. Chem. Phys.*, 2006, **124**, 174104.

27 A. Tkatchenko and M. Scheffler, *Phys. Rev. Lett.*, 2009, **102**, 073005.

28 A. Tkatchenko, R. A. DiStasio, R. Car and M. Scheffler, *Phys. Rev. Lett.*, 2012, **108**, 236402.

29 M. Bursch, J.-M. Mewes, A. Hansen and S. Grimme, *Angew. Chemie*, 2022, **134**, e202205735.

30 N. Jacob, Y. Zaid, J. C. A. Oliveira, L. Ackermann and J. Wencel-Delord, *J. Am. Chem. Soc.*, 2022, **144**, 798–806.

31 S. Ehlert, U. Huniar, J. Ning, J. W. Furness, J. Sun, A. D. Kaplan, J. P. Perdew and J. G. Brandenburg, *J. Chem. Phys.*, 2021, **154**, 061101.

32 A. Najibi and L. Goerigk, *J. Comput. Chem.*, 2020, **41**, 2562–2572.

33 L. Wittmann, H. Neugebauer, S. Grimme and M. Bursch, *J. Chem. Phys.*, 2023, **159**, 224103.

34 C. Plett, A. Katbashev, S. Ehlert, S. Grimme and M. Bursch, *Phys. Chem. Chem. Phys.*, 2023, **25**, 17860–17868.

35 E. Caldeweyher and J. G. Brandenburg, *J. Phys.: Condens. Matter*, 2018, **30**, 213001.

36 R. Sure and S. Grimme, *J. Comput. Chem.*, 2013, **34**, 1672–1685.

37 J. G. Brandenburg, C. Bannwarth, A. Hansen and S. Grimme, *J. Chem. Phys.*, 2018, **148**, 064104.

38 J. G. Brandenburg, E. Caldeweyher and S. Grimme, *Phys. Chem. Chem. Phys.*, 2016, **18**, 15519–15523.

39 S. Grimme, J. G. Brandenburg, C. Bannwarth and A. Hansen, *J. Chem. Phys.*, 2015, **143**, 054107.

40 S. Grimme, A. Hansen, S. Ehlert and J.-M. Mewes, *J. Chem. Phys.*, 2021, **154**, 064103.

41 M. Müller, A. Hansen and S. Grimme, *J. Chem. Phys.*, 2023, **158**, 014103.

42 T. Bredow and K. Jug, *Theor. Chem. Acc.*, 2004, **113**, 1–14.

43 W. Thiel, *Wiley Interdiscip. Rev.: Comput. Mol. Sci.*, 2013, **4**, 145–157.

44 A. S. Christensen, T. Kubáč, Q. Cui and M. Elstner, *Chem. Rev.*, 2016, **116**, 5301–5337.

45 C. Bannwarth, E. Caldeweyher, S. Ehlert, A. Hansen, P. Pracht, J. Seibert, S. Spicher and S. Grimme, *Wiley Interdiscip. Rev.: Comput. Mol. Sci.*, 2021, **11**, e1493.

46 S. Grimme, C. Bannwarth and P. Shushkov, *J. Chem. Theory Comput.*, 2017, **13**, 1989–2009.

47 C. Bannwarth, S. Ehlert and S. Grimme, *J. Chem. Theory Comput.*, 2019, **15**, 1652–1671.

48 P. Pracht, F. Böhle and S. Grimme, *Phys. Chem. Chem. Phys.*, 2020, **22**, 7169–7192.

49 P. Pracht, S. Grimme, C. Bannwarth, F. Böhle, S. Ehlert, G. Feldmann, J. Gorges, M. Müller, T. Neudecker, C. Plett, S. Spicher, P. Steinbach, P. A. Wesołowski and F. Zeller, *J. Chem. Phys.*, 2024, **160**, 114110.

50 S. Dohm, M. Bursch, A. Hansen and S. Grimme, *J. Chem. Theory Comput.*, 2020, **16**, 2002–2012.

51 L. W. Chung, W. M. C. Sameera, R. Ramozzi, A. J. Page, M. Hatanaka, G. P. Petrova, T. V. Harris, X. Li, Z. Ke, F. Liu, H.-B. Li, L. Ding and K. Morokuma, *Chem. Rev.*, 2015, **115**, 5678–5796.

52 C. E. Tzeliou, M. A. Mermigki and D. Tzeli, *Molecules*, 2022, **27**, 2660.

53 B. Pullman, *Isr. J. Chem.*, 1975, **14**, 69–78.

54 C. F. Matta, *Quantum biochemistry*, John Wiley & Sons, 2010.

55 Q. Cui, *J. Chem. Phys.*, 2016, **145**, 140901.

56 J.-C. G. Bunzli and V. K. Pecharsky, *Handbook on the Physics and Chemistry of Rare Earths: Including Actinides*, Elsevier, 2016.

57 R. E. Wilson, S. De Sio and V. Vallet, *Nat. Commun.*, 2018, **9**, 622.

58 J. Veliscek-Carolan, *J. Hazard. Mater.*, 2016, **318**, 266–281.



59 J. A. Laub and K. D. Vogiatzis, *J. Phys. Chem. A*, 2023, **127**, 5523–5533.

60 A. Francis, *J. Alloys Compd.*, 1998, **271–273**, 78–84.

61 R. C. Ewing, *Proc. Natl. Acad. Sci. U. S. A.*, 1999, **96**, 3432–3439.

62 R. C. Thompson, *Radiat. Res.*, 1982, **90**, 1.

63 K. Maher, J. R. Bargar and G. E. Brown, *Inorg. Chem.*, 2012, **52**, 3510–3532.

64 J. Suh, *Acc. Chem. Res.*, 1992, **25**, 273–279.

65 Y.-W. Lin, *Molecules*, 2019, **24**, 2743.

66 S. Safi, M. C. Charbonnel, G. Creff, A. Jeanson, S. Mostapha, J. Roques, E. Simoni, P. Solari, C. Vidaud and C. Den Auwer, *MRS Online Proc. Libr.*, 2012, **1444**, mrss12–1444.

67 A. Garai and P. Delangle, *J. Inorg. Biochem.*, 2020, **203**, 110936.

68 J. G. Hamilton, *Rev. Mod. Phys.*, 1948, **20**, 718–728.

69 E. Ansoborlo, O. Prat, P. Moisy, C. Den Auwer, P. Guilbaud, M. Carriere, B. Gouget, J. Duffield, D. Doizi, T. Vercouter, C. Moulin and V. Moulin, *Biochimie*, 2006, **88**, 1605–1618.

70 É. Ansoborlo, B. Amekraz, C. Moulin, V. Moulin, F. Taran, T. Baily, R. Burgada, M.-H. Hengé-Napoli, A. Jeanson, C. Den Auwer, L. Bonin and P. Moisy, *C. R. Chim.*, 2007, **10**, 1010–1019.

71 G. Creff, C. Zurita, A. Jeanson, G. Carle, C. Vidaud and C. Den Auwer, *Radiochim. Acta*, 2019, **107**, 993–1009.

72 S. Y. Tolmachev, M. E. Ketterer, D. Hare, P. Doble and A. C. James, *Proc. Radiochem.*, 2011, **1**, 173–181.

73 E. Vergucht, B. De Samber, A. Izmer, B. Vekemans, K. Appel, S. Tolmachev, L. Vincze and F. Vanhaecke, *Anal. Bioanal. Chem.*, 2014, **407**, 1559–1566.

74 R. Bulman, *Coord. Chem. Rev.*, 1980, **31**, 221–250.

75 D. Hare, S. Tolmachev, A. James, D. Bishop, C. Austin, F. Fryer and P. Doble, *Anal. Chem.*, 2010, **82**, 3176–3182.

76 N. Archipowa, L. Wittmann, J. Köckenberger, F. J. Ertl, J. Gleixner, M. Keller, M. R. Heinrich and R. J. Kutta, *J. Phys. Chem. B*, 2023, **127**, 9532–9542.

77 R. M. Pallares and R. J. Abergel, *Nanoscale*, 2020, **12**, 1339–1348.

78 S. J. Goldsmith, *Semin. Nucl. Med.*, 1975, **5**, 125–152.

79 E. R. Birnbaum, M. E. Fassbender, M. G. Ferrier, K. D. John and T. Mastren, *The Heaviest Metals: Science and Technology of the Actinides and Beyond*, 2019, p. 445.

80 T. I. Kostelnik and C. Orvig, *Chem. Rev.*, 2018, **119**, 902–956.

81 I. Kopp, P. Cieslik, K. Anger, T. Josephy, L. Neupert, G. Velmurugan, M. Gast, H. Wadeohl, S. A. Brühlmann, M. Walther, K. Kopka, M. Bachmann, H. Stephan, M. Kubel and P. Comba, *Inorg. Chem.*, 2023, **62**, 20754–20768.

82 N. Kaltsoyannis, *Chem. Soc. Rev.*, 2002, **32**, 9–16.

83 G. Schreckenbach and G. A. Shamov, *Acc. Chem. Res.*, 2009, **43**, 19–29.

84 A. J. Freeman and J. B. Darby, *The actinides: Electronic structure and related properties*, Academic Press, 1974.

85 V. Cocalia, K. Gutowski and R. Rogers, *Coord. Chem. Rev.*, 2006, **250**, 755–764.

86 X.-D. Wen, R. L. Martin, G. E. Scuseria, S. P. Rudin and E. R. Batista, *J. Phys. Chem. C*, 2013, **117**, 13122–13128.

87 X.-D. Wen, R. L. Martin, T. M. Henderson and G. E. Scuseria, *Chem. Rev.*, 2012, **113**, 1063–1096.

88 A. Kovács, R. J. M. Konings, J. K. Gibson, I. Infante and L. Gagliardi, *Chem. Rev.*, 2015, **115**, 1725–1759.

89 P. Grover, M. S. Oakley and G. Schreckenbach, *J. Phys. Chem. C*, 2024, **128**, 3033–3042.

90 L. Belkhiri, B. Le Guennic and A. Boucekkine, *Magnetochimistry*, 2019, **5**, 15.

91 P. Söderlind, G. Kotliar, K. Haule, P. M. Oppeneer and D. Guillaumont, *MRS Bull.*, 2010, **35**, 883–888.

92 A. Golovkina, D. Ovsyannikov and S. Olaru, *Cybern. Phys.*, 2018, 210–215.

93 M. S. Christian, E. R. Johnson and T. M. Besmann, *J. Phys. Chem. A*, 2021, **125**, 2791–2799.

94 S. Grimme, A. Hansen, J. G. Brandenburg and C. Bannwarth, *Chem. Rev.*, 2016, **116**, 5105–5154.

95 S. Grimme, *Wiley Interdiscip. Rev.: Comput. Mol. Sci.*, 2011, **1**, 211–228.

96 A. Salam, *Non-Relativistic QED Theory of the van der Waals Dispersion Interaction*, Springer International Publishing, 2016.

97 S. Grimme, S. Ehrlich and L. Goerigk, *J. Comput. Chem.*, 2011, **32**, 1456–1465.

98 J.-D. Chai and M. Head-Gordon, *Phys. Chem. Chem. Phys.*, 2008, **10**, 6615.

99 P. Xu, M. Alkan and M. S. Gordon, *Chem. Rev.*, 2020, **120**, 12343–12356.

100 S. M. Gatica, M. M. Calbi, M. W. Cole and D. Velegol, *Phys. Rev. B: Condens. Matter Mater. Phys.*, 2003, **68**, 205409–205417.

101 O. Anatole von Lilienfeld and A. Tkatchenko, *J. Chem. Phys.*, 2010, **132**, 234109–234120.

102 S. Grimme, *J. Comput. Chem.*, 2006, **27**, 1787–1799.

103 H. B. G. Casimir and D. Polder, *Phys. Rev.*, 1948, **73**, 360–372.

104 B. M. Axilrod and E. Teller, *J. Chem. Phys.*, 1943, **11**, 299–300.

105 Y. Muto, *Nippon Sugaku-Buturigakkaiishi*, 1943, **17**, 629–631.

106 H. Schröder, A. Creon and T. Schwabe, *J. Chem. Theory Comput.*, 2015, **11**, 3163–3170.

107 D. G. A. Smith, L. A. Burns, K. Patkowski and C. D. Sherrill, *J. Phys. Chem. Lett.*, 2016, **7**, 2197–2203.

108 J. Witte, N. Mardirossian, J. B. Neaton and M. Head-Gordon, *J. Chem. Theory Comput.*, 2017, **13**, 2043–2052.

109 D. C. Ghosh and N. Islam, *Int. J. Quantum Chem.*, 2009, **110**, 1206–1213.

110 S. A. Ghasemi, A. Hofstetter, S. Saha and S. Goedecker, *Phys. Rev. B: Condens. Matter Mater. Phys.*, 2015, **92**, 045131.

111 P. Norman, A. Jiemchooroj and B. E. Sernelius, *J. Chem. Phys.*, 2003, **118**, 9167–9174.

112 T. Saue and H. J. A. Jensen, *J. Chem. Phys.*, 2003, **118**, 522–536.



113 J. Kauczor, P. Jørgensen and P. Norman, *J. Chem. Theory Comput.*, 2011, **7**, 1610–1630.

114 J. Kauczor and P. Norman, *J. Chem. Theory Comput.*, 2014, **10**, 2449–2455.

115 P. W. Langhoff and M. Karplus, *J. Chem. Phys.*, 1970, **53**, 233–250.

116 F. Visser, P. E. S. Wormer and P. Stam, *J. Chem. Phys.*, 1983, **79**, 4973–4984.

117 P. W. Fowler, P. Jørgensen and J. Olsen, *J. Chem. Phys.*, 1990, **93**, 7256–7263.

118 S. Weiss and R. Egger, *Phys. Rev. B: Condens. Matter Mater. Phys.*, 2005, **72**, 245301–245307.

119 I. Kylänpää, J. Balachandran, P. Ganesh, O. Heinonen, P. R. C. Kent and J. T. Krogel, *Phys. Rev. Mater.*, 2017, **1**, 065408–065417.

120 J. Shee, S. Zhang, D. R. Reichman and R. A. Friesner, *J. Chem. Theory Comput.*, 2017, **13**(6), 2667–2680.

121 D. M. Bishop and J. Pipin, *Int. J. Quantum Chem.*, 1993, **45**, 349–361.

122 J. Mitroy, S. Bubin, W. Horiuchi, Y. Suzuki, L. Adamowicz, W. Cencek, K. Szalewicz, J. Komasa, D. Blume and K. Varga, *Rev. Mod. Phys.*, 2013, **85**, 693–749.

123 N. M. Tubman, I. Kylänpää, S. Hammes-Schiffer and D. M. Ceperley, *Phys. Rev. A: At., Mol., Opt. Phys.*, 2014, **90**, 042507–042512.

124 Y. Yang, I. Kylänpää, N. M. Tubman, J. T. Krogel, S. Hammes-Schiffer and D. M. Ceperley, *J. Chem. Phys.*, 2015, **143**, 124308–124318.

125 ORCA – an *ab initio*, density functional and semiempirical program package, V. 5.0.1, F. Neese, MPI für Kohlenforschung, Mülheim a. d. Ruhr (Germany), 2021.

126 F. Neese, *Wiley Interdiscip. Rev.: Comput. Mol. Sci.*, 2022, e1606.

127 K. Eichkorn, F. Weigend, O. Treutler and R. Ahlrichs, *Theor. Chem. Acc.*, 1997, **97**, 119–124.

128 J. Zheng, X. Xu and D. G. Truhlar, *Theor. Chem. Acc.*, 2010, **128**, 295–305.

129 C. Adamo and V. Barone, *J. Chem. Phys.*, 1999, **110**, 6158–6170.

130 F. L. Hirshfeld, *Theor. Chim. Acta*, 1977, **44**, 129–138.

131 N. Mardirossian and M. Head-Gordon, *J. Chem. Phys.*, 2016, **144**, 214110.

132 G. L. Stoychev, A. A. Auer and F. Neese, *J. Chem. Theory Comput.*, 2017, **13**, 554–562.

133 F. Neese, F. Wennmohs, A. Hansen and U. Becker, *Chem. Phys.*, 2009, **356**, 98–109.

134 R. Izsák and F. Neese, *J. Chem. Phys.*, 2011, **135**, 144105.

135 B. Helmich-Paris, B. de Souza, F. Neese and R. Izsák, *J. Chem. Phys.*, 2021, **155**, 104109.

136 D. Andrae, U. Häußermann, M. Dolg, H. Stoll and H. Preuß, *Theor. Chim. Acta*, 1990, **77**, 123–141.

137 K. A. Peterson, D. Figgen, E. Goll, H. Stoll and M. Dolg, *J. Chem. Phys.*, 2003, **119**, 11113–11123.

138 J. P. Perdew, K. Burke and M. Ernzerhof, *Phys. Rev. Lett.*, 1996, **77**, 3865–3868.

139 E. Caldeweyher, S. Ehler, A. Hansen, H. Neugebauer, S. Spicher, C. Bannwarth and S. Grimme, *J. Chem. Phys.*, 2019, **150**, 154122.

140 K. G. Dyall, *Theor. Chem. Acc.*, 2007, **117**, 491.

141 K. G. Dyall, *Theor. Chem. Acc.*, 2012, **131**, 1217.

142 written by H. J. A. Jensen, R. Bast, A. S. P. Gomes, T. Saue and L. Visscher, with contributions from, I. A. Aucar, V. Bakken, C. Chibueze, J. Creutzberg, K. G. Dyall, S. Dubillard, U. Ekström, E. Eliav, T. Enevoldsen, E. Faßhauer, T. Fleig, O. Fossgaard, L. Halbert, E. D. Hedegård, T. Helgaker, B. Helmich-Paris, J. Henriksson, M. van Horn, M. Iliaš, C. R. Jacob, S. Knecht, S. Komorovský, O. Kullie, J. K. Lærdahl, C. V. Larsen, Y. S. Lee, N. H. List, H. S. Nataraj, M. K. Nayak, P. Norman, G. Olejniczak, J. Olsen, J. M. H. Olsen, A. Papadopoulos, Y. C. Park, J. K. Pedersen, M. Pernpointner, J. V. Pototschnig, R. di Remigio, M. Repisky, K. Ruud, P. Sałek, B. Schimmelpfennig, B. Senjean, A. Shee, J. Sikkema, A. Sunaga, A. J. Thorvaldsen, J. Thyssen, J. van Stralen, M. L. Vidal, S. Villaume, O. Visser, T. Winther, S. Yamamoto and X. Yuan, *DIRAC, a relativistic *ab initio* electronic structure program, Release DIRAC22*, 2022, DOI: [10.5281/zenodo.6010450](https://doi.org/10.5281/zenodo.6010450), see also <https://www.diracprogram.org>.

143 L. Trombach, S. Ehler, S. Grimme, P. Schwerdtfeger and J.-M. Mewes, *Phys. Chem. Chem. Phys.*, 2019, **21**, 18048–18058.

144 P. Jerabek, O. R. Smits, J.-M. Mewes, K. A. Peterson and P. Schwerdtfeger, *J. Phys. Chem. A*, 2019, **123**, 4201–4211.

145 O. R. Smits, J. Mewes, P. Jerabek and P. Schwerdtfeger, *Angew. Chem., Int. Ed.*, 2020, **59**, 23636–23640.

146 P. Pyykkö and M. Atsumi, *Chem. – Eur. J.*, 2008, **15**, 186–197.

147 A. Allred, *J. Inorg. Nucl. Chem.*, 1961, **17**, 215–221.

148 A. F. Holleman, *Lehrbuch der Anorganischen Chemie*, De Gruyter, 1964, p. 2146.

149 J. Huheey, E. Keiter, R. Keiter and O. Medhi, *Inorganic Chemistry: Principles of Structure and Reactivity*, Pearson Education, 2006.

150 L. C. Allen, *J. Am. Chem. Soc.*, 1989, **111**, 9003–9014.

151 A. Allred, *J. Inorg. Nucl. Chem.*, 1961, **17**, 215–221.

152 M. G. Taylor, D. J. Burrill, J. Janssen, E. R. Batista, D. Perez and P. Yang, *Nat. Commun.*, 2023, **14**, 2786.

153 Architector, <https://github.com/lanl/Architector>.

154 ArchitectorWrapper, <https://github.com/grimme-lab/ArchitectorWrapper>.

155 C. Hölzer, I. Gordiy, S. Grimme and M. Bursch, *J. Chem. Inf. Model.*, 2024, **64**, 825–836.

156 M. Korth and S. Grimme, *J. Chem. Theory Comput.*, 2009, **5**, 993–1003.

157 J. A. Nelder and R. Mead, *Comput. J.*, 1965, **7**, 308–313.

158 M. H. Wright, *Direct Search Methods: Once Scorned, Now Respectable*, Addison Wesley Longman, Harlow, United Kingdom, 1996, pp. 191–208.

159 S. Ehrlich, J. Moellmann and S. Grimme, *Acc. Chem. Res.*, 2012, **46**, 916–926.

160 S. Grimme, A. Hansen, J. G. Brandenburg and C. Bannwarth, *Chem. Rev.*, 2016, **116**, 5105–5154.



161 W. Hujo and S. Grimme, *J. Chem. Theory Comput.*, 2011, **7**, 3866–3871.

162 W. Hujo and S. Grimme, *J. Chem. Theory Comput.*, 2012, **9**, 308–315.

163 L. Goerigk, *J. Chem. Theory Comput.*, 2014, **10**, 968–980.

164 M. A. Iron and T. Janes, *J. Phys. Chem. A*, 2019, **123**, 3761–3781.

165 T. Risthaus and S. Grimme, *J. Chem. Theory Comput.*, 2013, **9**, 1580–1591.

166 D. E. Taylor, J. G. Ángyán, G. Galli, C. Zhang, F. Gygi, K. Hirao, J. W. Song, K. Rahul, O. A. von Lilienfeld, R. Podeszwa, I. W. Bulik, T. M. Henderson, G. E. Scuseria, J. Toulouse, R. Peverati, D. G. Truhlar and K. Szalewicz, *J. Chem. Phys.*, 2016, **145**, 124105.

167 J. Řezáč, K. E. Riley and P. Hobza, *J. Chem. Theory Comput.*, 2011, **7**, 2427–2438.

168 B. Brauer, M. K. Kesharwani, S. Kozuch and J. M. L. Martin, *Phys. Chem. Chem. Phys.*, 2016, **18**, 20905–20925.

169 G. Santra, E. Semidalas, N. Mehta, A. Karton and J. M. L. Martin, *Phys. Chem. Chem. Phys.*, 2022, **24**, 25555–25570.

170 P. Jurečka, J. Šponer, J. Černý and P. Hobza, *Phys. Chem. Chem. Phys.*, 2006, **8**, 1985–1993.

171 L. Gráfová, M. Pitoňák, J. Řezáč and P. Hobza, *J. Chem. Theory Comput.*, 2010, **6**, 2365–2376.

172 J. C. Sancho-García, A. J. Pérez-Jiménez and Y. Olivier, *J. Chem. Phys.*, 2015, **142**, 054702.

173 M. Bursch, S. Grimme and A. Hansen, *Acc. Chem. Res.*, 2023, **57**, 153–163.

174 A. D. Becke, *J. Chem. Phys.*, 1993, **98**, 5648–5652.

175 P. J. Stephens, F. J. Devlin, C. F. Chabalowski and M. J. Frisch, *J. Phys. Chem.*, 1994, **98**, 11623–11627.

176 G. Beridze and P. M. Kowalski, *J. Phys. Chem. A*, 2014, **118**, 11797–11810.

177 B. Weinstock and R. H. Crist, *J. Chem. Phys.*, 1948, **16**, 436–441.

178 H. M. Seip, J.-O. Lundgren, P. KlÃ¶be and T.-M. Enari, *Acta Chem. Scand.*, 1965, **19**, 1955–1968.

179 Y. S. Ezhov, S. A. Komarov, V. G. Sevastyanov and V. I. Bazhanov, *J. Struct. Chem.*, 1993, **34**, 473–474.

180 V. I. Bazhanov, Y. S. Ezhov and S. A. Komarov, *J. Struct. Chem.*, 1991, **31**, 986–987.

181 C. R. Groom, I. J. Bruno, M. P. Lightfoot and S. C. Ward, *Acta Crystallogr., Sect. B: Struct. Sci., Cryst. Eng. Mater.*, 2016, **72**, 171–179.

182 H. Neugebauer, H. T. Vuong, J. L. Weber, R. A. Friesner, J. Shee and A. Hansen, *J. Chem. Theory Comput.*, 2023, **19**, 6208–6225.

183 E. A. Coutsias, C. Seok and K. A. Dill, *J. Comput. Chem.*, 2004, **25**, 1849–1857.

184 H. Braunschweig, M. A. Celik, K. Dück, F. Hupp and I. Krummenacher, *Chem. – Eur. J.*, 2015, **21**, 9339–9342.

185 H. Braunschweig, M. A. Celik, K. Dück, F. Hupp and I. Krummenacher, CCDC 1047312: Experimental Crystal Structure Determination, 2015, https://www.ccdc.cam.ac.uk/services/structure_request?id=doi:10.5517/cc144t8csid=DataCite.

186 B. Allard, S. Dhabanandana, J. Krogh-Moe, J. Songstad and Å. Pilotti, *Acta Chem. Scand.*, 1972, **26**, 3492–3504.

187 N. W. Alcock and D. J. Flanders, *Acta Crystallogr., Sect. C: Cryst. Struct. Commun.*, 1987, **43**, 1480–1483.

188 M. Lenner, *Acta Crystallogr., Sect. B: Struct. Sci., Cryst. Eng. Mater.*, 1979, **35**, 2396–2398.

189 S. Schöne, T. Radoske, J. März, T. Stumpf, M. Patzschke and A. Ikeda-Ohno, CCDC 1553027: Experimental Crystal Structure Determination, 2017, https://www.ccdc.cam.ac.uk/services/structure_request?id=doi:10.5517/ccdc.csd.cc1p41njsid=DataCite.

190 S. Schöne, T. Radoske, J. März, T. Stumpf, M. Patzschke and A. Ikeda-Ohno, *Chem. – Eur. J.*, 2017, **23**, 13574–13578.

191 S. Hohloch, M. E. Garner, B. F. Parker and J. Arnold, *Dalton Trans.*, 2017, **46**, 13768–13782.

192 S. Hohloch, M. E. Garner, B. F. Parker and J. Arnold, CCDC 1554548: Experimental Crystal Structure Determination, 2017, https://www.ccdc.cam.ac.uk/services/structure_request?id=doi:10.5517/ccdc.csd.cc1p5mq6 sid=DataCite.

193 S. Hohloch, M. E. Garner, B. F. Parker and J. Arnold, CCDC 1554554: Experimental Crystal Structure Determination, 2017, https://www.ccdc.cam.ac.uk/services/structure_request?id=doi:10.5517/ccdc.csd.cc1p5mxdsid=DataCite.

194 S. Hohloch, M. E. Garner, B. F. Parker and J. Arnold, *Dalton Trans.*, 2017, **46**, 13768–13782.

195 S. S. Galley, J. M. Sperling, C. J. Windorff, M. Zeller, T. E. Albrecht-Schmitt and S. C. Bart, CCDC 1557708: Experimental Crystal Structure Determination, 2019, https://www.ccdc.cam.ac.uk/services/structure_request?id=doi:10.5517/ccdc.csd.cc1p8xnjsid=DataCite.

196 S. S. Galley, J. M. Sperling, C. J. Windorff, M. Zeller, T. E. Albrecht-Schmitt and S. C. Bart, *Organometallics*, 2019, **38**, 606–609.

197 S. K. Cary, J. Su, S. S. Galley, T. E. Albrecht-Schmitt, E. R. Batista, M. G. Ferrier, S. A. Kozimor, V. Mocko, B. L. Scott, C. E. Van Alstine, F. D. White and P. Yang, CCDC 1841778: Experimental Crystal Structure Determination, 2018, https://www.ccdc.cam.ac.uk/services/structure_request?id=doi:10.5517/ccdc.csd.cc1ztj6jsid=DataCite.

198 S. K. Cary, J. Su, S. S. Galley, T. E. Albrecht-Schmitt, E. R. Batista, M. G. Ferrier, S. A. Kozimor, V. Mocko, B. L. Scott, C. E. Van Alstine, F. D. White and P. Yang, *Dalton Trans.*, 2018, **47**, 14452–14461.

199 M. L. Tarlton, S. Skanthakumar, V. Vallet and R. E. Wilson, CCDC 2168159: Experimental Crystal Structure Determination, 2022, https://www.ccdc.cam.ac.uk/services/structure_request?id=doi:10.5517/ccdc.csd.cc2bs4mksid=DataCite.

200 M. L. Tarlton, S. Skanthakumar, V. Vallet and R. E. Wilson, *Chem. Commun.*, 2022, **58**, 11997–12000.

201 L. Serezhkina, E. Peresypkina, A. Virovets and N. Neklyudova, CCDC 713927: Experimental Crystal Structure Determination, 2011, https://www.ccdc.cam.ac.uk/services/structure_request?id=doi:10.5517/crywxtgsid=DataCite.

202 L. B. Serezhkina, E. V. Peresypkina, A. V. Virovets and N. A. Neklyudova, *Russ. J. Inorg. Chem.*, 2010, **55**, 1020–1025.



203 L. B. Serezhkina, E. V. Peresypkina, Y. A. Medvedkov, A. V. Virovets and V. N. Serezhkin, *Russ. J. Inorg. Chem.*, 2013, **58**, 1465–1469.

204 N. N. Krot, I. A. Charushnikova, M. S. Grigor'ev, A. A. Bessonov and I. N. Polyakova, *CCDC 726784: Experimental Crystal Structure Determination*, 2011, [DataCite](https://www.ccdc.cam.ac.uk/services/structure_request?id=doi:10.5517/ccsd8n2sid>DataCite.</p>
<p>205 N. N. Krot, I. A. Charushnikova, M. S. Grigorev, A. A. Bessonov and I. N. Polyakova, <i>Radiochemistry</i>, 2010, 52, 12–16.</p>
<p>206 T. Kawasaki, T. Nishimura and T. Kitazawa, <i>CCDC 793245: Experimental Crystal Structure Determination</i>, 2011, <a href=).

207 T. Kawasaki, T. Nishimura and T. Kitazawa, *Bull. Chem. Soc. Jpn.*, 2010, **83**, 1528–1530.

208 B. E. Allred, P. B. Rupert, S. S. Gauny, D. D. An, C. Y. Ralston, M. Sturzbecher-Hoehne, R. K. Strong and R. J. Abergel, *Proc. Natl. Acad. Sci. U. S. A.*, 2015, **112**, 10342–10347.

209 B. Allred, P. Rupert, S. Gauny, D. An, C. Ralston, M. Sturzbecher-Hoehne, R. Strong and R. Abergel, Siderocalin-mediated recognition and cellular uptake of actinides, 2015, DOI: [10.2210/pdb4ZHF/pdb](https://doi.org/10.2210/pdb4ZHF/pdb).

210 C. Zardecki, S. Dutta, D. S. Goodsell, R. Lowe, M. Voigt and S. K. Burley, *Protein Sci.*, 2021, **31**, 129–140.

211 H. M. Berman, *Nucleic Acids Res.*, 2000, **28**, 235–242.

212 A. Hansen, C. Bannwarth, S. Grimme, P. Petrović, C. Werlé and J.-P. Djukic, *ChemistryOpen*, 2014, **3**, 177–189.

213 Q. Lu, F. Neese and G. Bistoni, *Phys. Chem. Chem. Phys.*, 2019, **21**, 11569–11577.

214 M. Bursch, E. Caldeweyher, A. Hansen, H. Neugebauer, S. Ehlert and S. Grimme, *Acc. Chem. Res.*, 2019, **52**, 258–266.

215 J. B. A. Davis, F. Baletto and R. L. Johnston, *J. Phys. Chem. A*, 2015, **119**, 9703–9709.

216 R. Hatz, V. Hänninen and L. Halonen, *J. Phys. Chem. A*, 2014, **118**, 5734–5740.

217 G. Pacchioni, *Phys. Chem. Chem. Phys.*, 2013, **15**, 1737–1757.

218 R. J. Maurer, V. G. Ruiz and A. Tkatchenko, *J. Chem. Phys.*, 2015, **143**, 102808.

219 F. R. Rehak, G. Piccini, M. Alessio and J. Sauer, *Phys. Chem. Chem. Phys.*, 2020, **22**, 7577–7585.

220 A. A. Adeleke and E. R. Johnson, *Phys. Rev. B*, 2023, **107**, 064101.

221 K. Tonigold and A. Groß, *J. Comput. Chem.*, 2012, **33**, 695–701.

222 X. Zhang, W. Li, L. Feng, X. Chen, A. Hansen, S. Grimme, S. Fortier, D.-C. Sergentu, T. J. Duignan, J. Autschbach, S. Wang, Y. Wang, G. Velkos, A. A. Popov, N. Aghdassi, S. Duhm, X. Li, J. Li, L. Echegoyen, W. H. E. Schwarz and N. Chen, *Nat. Commun.*, 2018, **9**, 2753.

